Global optical model potential for the weakly bound projectile ^{9}Be

Yongli Xu,[1,*] Yinlu Han,[2,†] Haiying Liang,[2] Zhendong Wu,[2] Hairui Guo,[3] and Chonghai Cai[4]
[1]*College of Physics and Electronic Science, Shanxi Datong University, Datong 037009, China*
[2]*Key Laboratory of Nuclear Data, China Institute of Atomic Energy, P.O. Box (275-41), Beijing 102413, China*
[3]*Institute of Applied Physics and Computational Mathematics, Beijing 100094, China*
[4]*Department of Physics, Nankai University, Tianjin 300071, China*

(Received 7 November 2018; revised manuscript received 27 February 2019; published 29 March 2019)

The global optical model potential for the ^{9}Be projectile is developed by systematically studying the experimental data of elastic-scattering angular distributions and reaction cross sections from ^{24}Mg to ^{209}Bi below 100 MeV. The analysis is performed in terms of comparing the theoretical results with the available experimental data. A satisfactory agreement is observed in the whole energy and target mass regions. Moreover, the elastic-scattering angular distributions and reaction cross sections of ^{9}Be on some lighter targets are also predicted using the global optical model potential and a reasonable description of the experimental data is obtained.

DOI: 10.1103/PhysRevC.99.034618

I. INTRODUCTION

The study of a reaction mechanism involving light weakly bound projectiles, both stable and radioactive, is a topic of great interest in nuclear physics research nowadays. In the process of investigation, the phenomenological optical model potential (OMP) is an invaluable tool and often adopted to describe the elastic scattering [1]. In addition, the phenomenological OMP is also a very important input for other reaction mechanisms. For example, the optical potential giving a good description of the elastic scattering is needed for the calculations of transfer process, etc. So, the choice of the appropriate optical potential is a critical point when one wants to describe the elastic scattering data well with theory.

It is well known that the local phenomenological OMP for one nucleus at a particular energy reflects the peculiarities of that nucleus and may not be suitable for neighboring nuclei at different energies. However, the global phenomenological OMP specified for both mass and energy regions can reliably predict the elastic scattering observables in those regions where no measurements exist [2]. Therefore, it is essential to investigate the reliable global OMPs for use in the analysis of reaction mechanisms involving some light weakly bound projectiles.

For stable weakly bound projectile ^{9}Be, it is also of interest to both experimental and theoretical nuclear physicists. Since its decay into ^{8}Be and a neutron has a Q value of only -1.665 MeV, it is also a good tool for nuclear spectroscopy. In the process of studying the reactions involving ^{9}Be, the OMP is widely applied to the investigation of different reaction mechanisms [3,4]. So far, there is only one global OMP of ^{9}Be projectile which is obtained by fitting the experimental data of angular distributions for a few targets at incident energies of 14, 20, and 26 MeV [5]. However, the few and old data of elastic-scattering angular distributions considered in the fitting may lead to a large uncertainty of the global OMP parameters.

In recent years, the availability of radioactive ion beams has been further renewed and many experiments have been made to measure elastic scattering observables of weakly bound projectile ^{9}Be on various targets. Therefore, it is enough to investigate a new set of ^{9}Be global OMP parameters by optimizing descriptions of elastic-scattering angular distributions and reaction cross sections over a wide range of incident energies and target masses.

In this paper we report a new global phenomenological OMP of weakly bound projectile ^{9}Be by fitting the experimental elastic-scattering angular distributions and reaction cross sections from ^{24}Mg to ^{209}Bi targets at incident energies below 100 MeV. Furthermore, these elastic scattering observables for some targets outside of the mass range are predicted using the present global OMP.

The organization of this paper is as follows. In Sec. II, the method and formalism used in the present work are described in detail. Also, a new set of ^{9}Be global OMP parameters is presented in this section. In Sec. III, the comparisons of theoretical calculations with experimental data are exhibited and the discussions on the results are made. Finally, we present a summary of the results and the conclusions for this study in Sec. IV.

II. THE GLOBAL PHENOMENOLOGICAL OPTICAL MODEL POTENTIAL AND PARAMETERS

A. Form of the optical model potential

The optical potential used for the description of the elastic scattering is defined as

$$V(r,E) = V_R(r,E) + i[W_S(r,E) + W_V(r,E)] + V_C(r), \quad (1)$$

*xuyongli776@126.com
†hanyl@ciae.ac.cn

TABLE I. The $d\sigma/d\Omega$ database for ^{9}Be elastic scattering. The E is the incident energy for different targets in the laboratory system.

Target	E (MeV)	Ref.
^{nat}Mg	14.0,20.0,26.0	[5]
^{27}Al	12.0,14.0,18.0,22.0,25.0,28.0,32.0,33.0,35.0.40.0,47.5	[6]
	20.0	[5]
^{28}Si	12.0,14.0,17.0,20.0,23.0,26.0,30.0	[7]
	13.0	[8]
	45.0,60.0	[9]
	50.0	[10]
^{40}Ca	14.0,20.0,26.0	[5]
	45.0,60.0	[9]
	50.0	[10]
^{58}Ni	20.0,26.0	[5]
^{64}Zn	17.0,19.0,21.0,23.0,26.0,28.0	[11]
	28.4	[12]
	28.97	[13]
^{89}Y	18.6,20.6,22.7,24.7,26.7,28.7,33.2	[14]
^{nat}Ag	26.0	[5]
^{144}Sm	30.0,31.5,44.0,48.0	[15]
	33.0,34.0,35.0,37.0,39.0,41.0	[16]
^{208}Pb	38.0,40.0,42.0,44.0,46.0,48.0,50.0,60.0,68.0,75.0	[17]
	37.0,37.8,38.0,38.2,38.5,38.7,39.0,39.5,40.0,41.0	
	42.0,44.0,47.2,50.0	[18]
^{209}Bi	37.0,37.8,38.0,38.2,38.5,38.7,39.0,39.5,40.0,41.0	
	42.0,44.0	[18]
	40.0,42.0,44.0,46.0,48.0	[19]

where V_R stands for the real part of potential, W_S and W_V are the surface and volume imaginary parts of potential, respectively. $V_C(r)$ is the Coulomb potential.

As described in Ref. [31], the Woods-Saxon function is chosen for the form factors of real and imaginary potentials. They are respectively expressed as

$$V_R(r,E) = -\frac{V_R(E)}{1+\exp[(r-R_R)/a_R]}, \tag{2}$$

$$W_S(r,E) = -4W_S(E)\frac{\exp[(r-R_S)/a_S]}{\{1+\exp[(r-R_S)/a_S]\}^2}, \tag{3}$$

$$W_V(r,E) = -\frac{W_V(E)}{1+\exp[(r-R_V)/a_V]}. \tag{4}$$

The Coulomb potential V_C is assumed to be that of a uniformly charged sphere with a charge number Z of target and a radius R_C. It is approximately expressed by

$$V_C(r) = \begin{cases} \frac{zZe^2}{2R_C}\left(3-\frac{r^2}{R_C^2}\right) & r < R_C, \\ \frac{zZe^2}{r} & r \geqslant R_C, \end{cases} \tag{5}$$

where z is the charge number of the ^{9}Be projectile.

The energy-dependent potential depths have the following expressions:

$$V_R(E) = V_0 + V_1E + V_2E^2, \tag{6}$$

$$W_S(E) = \max\{0, W_0 + W_1E\}, \tag{7}$$

$$W_V(E) = \max\{0, U_0 + U_1E\}. \tag{8}$$

The radius R_i is defined as

$$R_i = r_iA^{\frac{1}{3}}, \quad i = R, S, V, C, \tag{9}$$

where A is target mass numbers. r_R, r_S, r_V, and r_C are, respectively, the radius parameters of real, surface and volume imaginary, and Coulomb potentials. The corresponding diffuseness parameters are a_R, a_S, and a_V. Especially, the radius parameter of the real potential is defined by

$$r_R = r_{R_0} + r_{R_1}A^{\frac{1}{3}}. \tag{10}$$

The adjusted parameters are V_0, V_1, V_2, W_0, W_1, U_0, U_1, r_{R_0}, r_{R_1}, r_S, r_V, r_C, a_R, a_S, and a_V.

The spin-orbit potential is not implemented in the parametrization of the ^{9}Be global OMP. The reason is that the experimental data of elastic-scattering angular distributions and reaction cross sections analyzed in this work are not sensitive to the spin-orbit potential.

B. Parametrization of the optical model potential

We have collected all the data of elastic-scattering angular distributions and reaction cross sections for those targets in the mass number range from 24 to 209 at incident ^{9}Be energies below 100 MeV. No measurements of elastic-scattering angular distributions were performed for these targets at higher energies. The details of these data are shown in Tables I and II.

All the experimental data of elastic angular distributions and reaction cross sections from ^{24}Mg to ^{209}Bi targets below 100 MeV are simultaneously fitting using the code APMN [26], which automatically searches optimal optical potential

TABLE II. The reaction cross sections database for ^{9}Be.

Target	Ref.
^{27}Al	[20,21]
^{28}Si	[7,22,23]
^{nat}Cu	[24]
^{64}Zn	[12,13]
^{89}Y	[25]
^{144}Sm	[15,16]

parameters below 300 MeV by the improved fastest falling method [27]. The global OMP parameters are optimized with the usual minimization of the χ^2 method. Following an approach similar to that in Ref. [31], the χ^2 for each single target is first obtained and then the average value of total χ^2 for all targets is founded, which is defined as

$$\chi^2 = \frac{1}{N}\sum_{i=1}^{N}\left[\frac{\sigma_i^{\rm th} - \sigma_i^{\rm exp}}{\Delta\sigma_i^{\rm exp}}\right]^2, \quad (11)$$

where σ_i are the elastic-scattering angular distributions or reaction cross sections, as well as $\Delta\sigma_i$ is the experimental error of corresponding data. The superscripts th and exp represent the theoretical and experimental values, respectively. N is the number of the considered nuclei.

Moreover, all the potential parameters reasonable boundaries of the varied region are given by some physical limitation before the global phenomenological OMP parameters are automatically searched. Using the above-mentioned optimization procedure, the parameters of global OMP for ^{9}Be projectile are obtained and listed in Table III.

III. CALCULATED RESULTS AND ANALYSIS

With the purpose to investigate the obtained global OMP of ^{9}Be, the radial dependence on the real part and imaginary part of global OMP are calculated using the obtained optimum parameters for different targets at incident energies of 20, 50, 100, 150, 200, 250, and 300 MeV, respectively. Figure 1 presents the results for the ^{58}Ni target. From the figure it is clearly seen that the depth of the real potential linearly decreases with increasing incident energy and also decreases with increasing radius. While the absolute value of the imaginary potential first increases and then decreases with increasing incident radius. Moreover, the contribution to the imaginary part of global OMP changes from the dominant surface absorption into the volume absorption with increasing incident energy.

TABLE III. The global phenomenological OMP parameters for ^{9}Be.

Parameter	Value	Unit
V_0	268.0671	MeV
V_1	−0.180	
V_2	−0.0009	
W_0	52.149	MeV
W_1	−0.125	
U_0	2.965	MeV
U_1	0.286	
r_{R_0}	1.200	fm
r_{R_1}	0.0273	fm
r_S	1.200	fm
r_V	1.640	fm
r_C	1.556	fm
a_R	0.726	fm
a_S	0.843	fm
a_V	0.600	fm

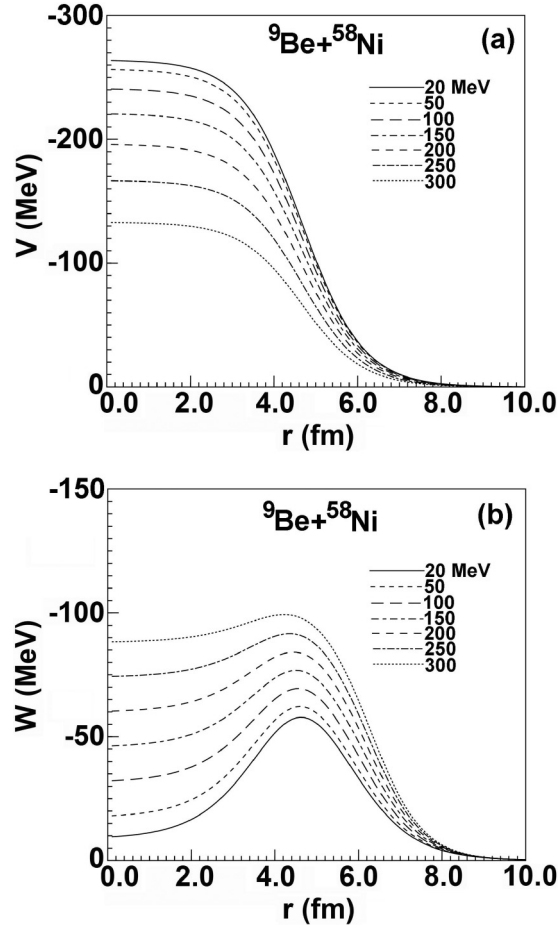

FIG. 1. The radial dependence of our global OMP at different incident energies for ^{58}Ni. (a) the real part; (b) the imaginary part.

Next, the elastic-scattering angular distributions are calculated using the obtained ^{9}Be global OMP for different targets. The detailed discussion is further made for the obtained global OMP by comparing between the theoretical results and the corresponding experimental data.

Figure 2 displays the elastic-scattering angular distributions for light mass target ^{24}Mg at incident energies of 14.0, 20.0, and 26.0 MeV. The results are compared with the experimental data from the ^{nat}Mg target [5]. A good fit is obtained between them. The elastic-scattering angular distributions of the ^{27}Al target are also calculated at incident energies from 12.0 to 47.5 MeV, which is shown in Fig. 3.

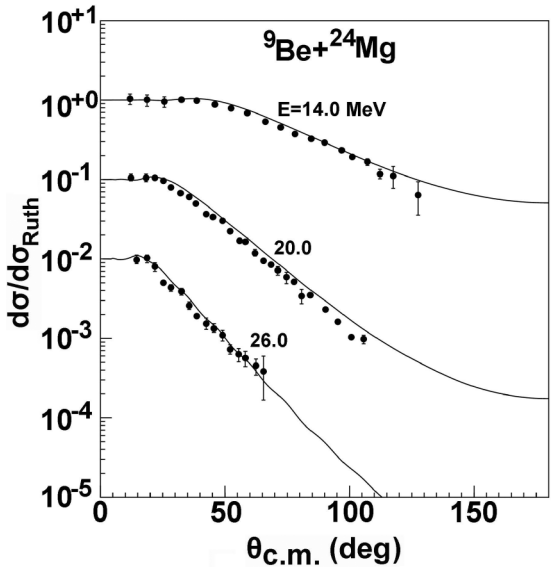

FIG. 2. Comparison between the optical model calculation and the experimental data [5] of ^{9}Be elastic-scattering angular distributions for ^{24}Mg.

Compared with the corresponding experimental data [5,6], the calculations almost fit all the experimental data very well except for few energy points deviating the systematic behavior at several angles.

For ^{28}Si, the comparisons of elastic-scattering angular distributions with the experimental data [7–10] are plotted in Fig. 4. The incident energy is from 12.0 to 60.0 MeV. It is seen that the calculations agree with the experimental data

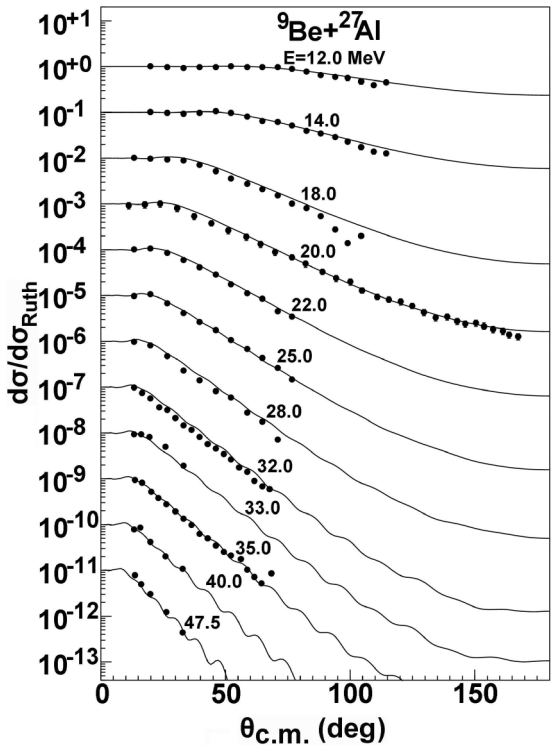

FIG. 3. The same as Fig. 2, but for ^{27}Al [5,6].

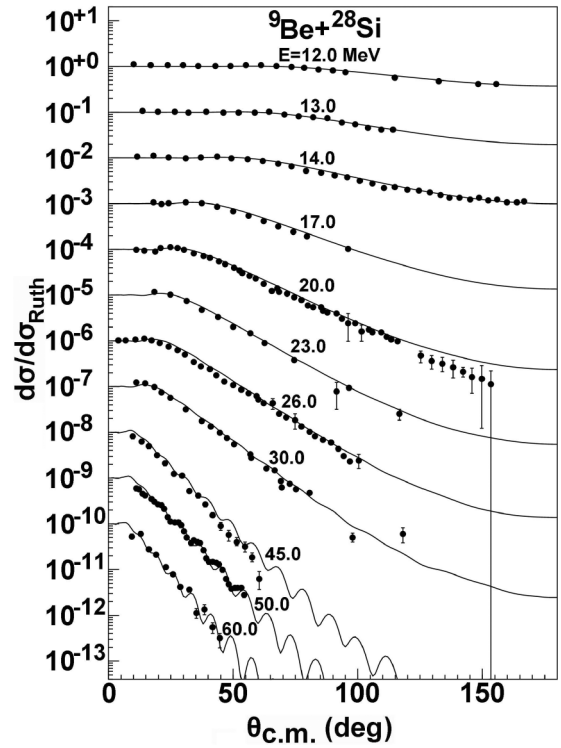

FIG. 4. The same as Fig. 2, but for ^{28}Si [7–10].

at these energies except for 20.0 MeV above 120°, where the calculations are smaller than the experimental data. The elastic-scattering angular distributions of ^{40}Ca are compared with the experimental data [5,9,10] at incident energies from 14.0 to 60.0 MeV. The results yield a good fit to the data except for 45.0 MeV above 70°, where the experimental data [9] has a sudden decline and deviates from the systematic behavior. The result is shown in Fig. 5.

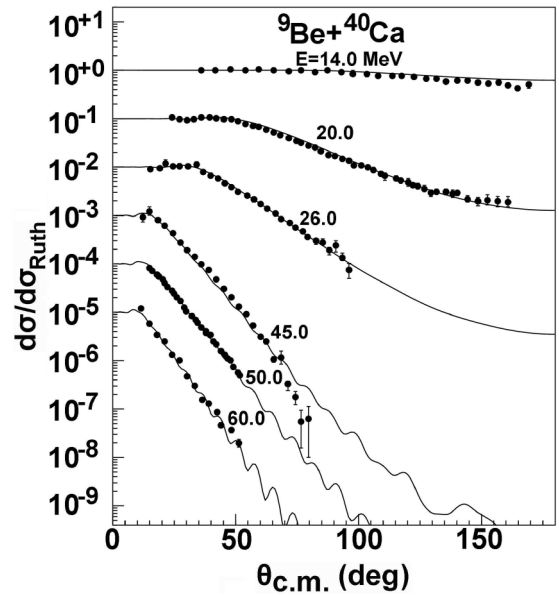

FIG. 5. The same as Fig. 2, but for ^{40}Ca [5,9,10].

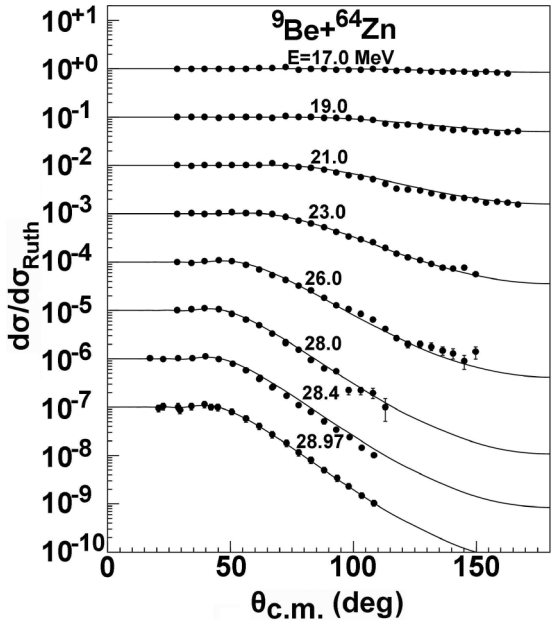

FIG. 6. The same as Fig. 2, but for ^{64}Zn [11–13].

The elastic-scattering angular distributions are calculated for the ^{64}Zn target at different incident energies. Figure 6 shows the comparisons between the calculations and the experimental data [11–13]. The excellent agreement is also obtained.

Moreover, the elastic angular distributions for medium mass target ^{89}Y are also compared with the data [14] between 18.6 and 33.2 MeV. The result is given in Fig. 7. From the figure one can see the calculations are in excellent agreement with the experimental data [14] in the whole incident energy range.

The elastic-scattering angular distributions for the ^{9}Be + ^{144}Sm system are calculated using the global OMP. The calculations along with the measured data [15,16] are displayed in Fig. 8. Comparisons with these data reveal that the set of optical potential parameters can describe the elastic-scattering angular distributions very well for ^{144}Sm over the entire energy range of the measurement.

For the ^{9}Be projectile on heavier mass target ^{208}Pb, the elastic-scattering angular distributions are also calculated using the global OMP. Figure 9 shows the comparison between

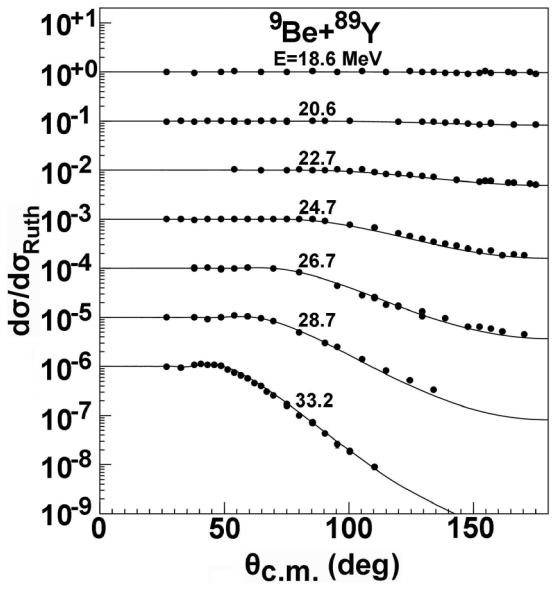

FIG. 7. The same as Fig. 2, but for ^{89}Y [14].

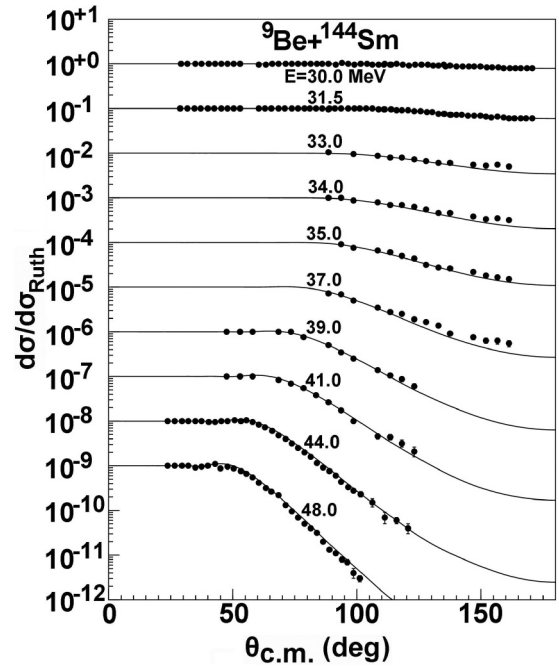

FIG. 8. The same as Fig. 2, but for ^{144}Sm [15,16].

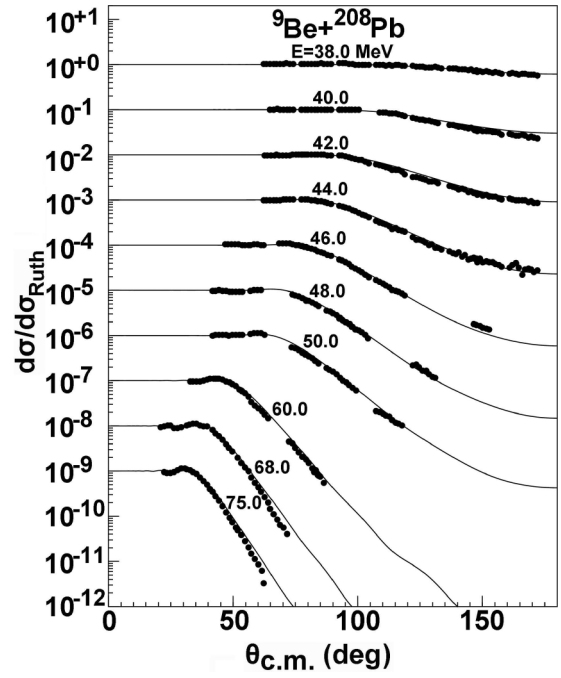

FIG. 9. The same as Fig. 2, but for ^{208}Pb [17].

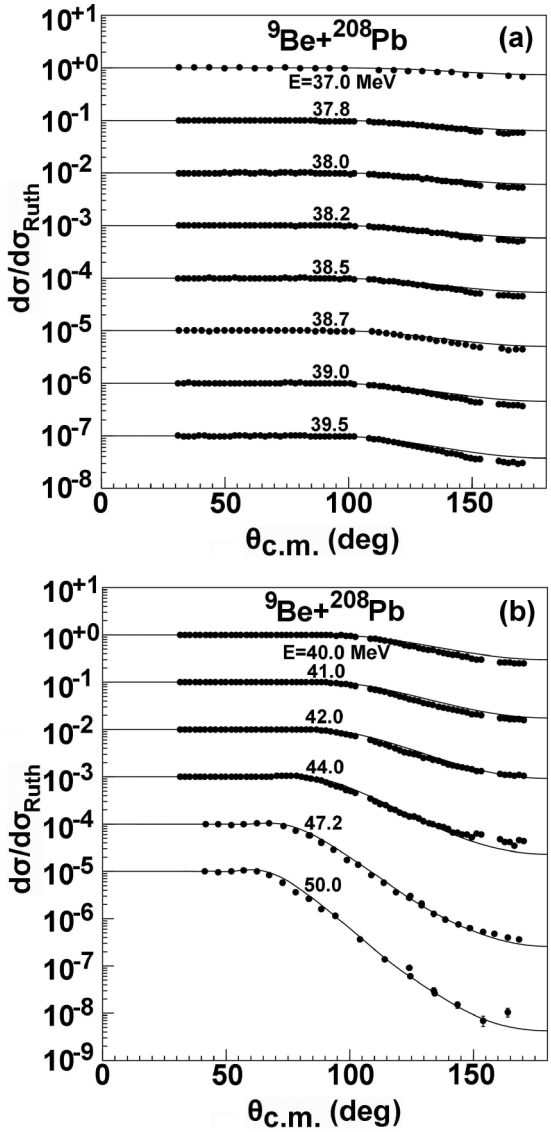

FIG. 10. The same as Fig. 2, but for ^{208}Pb [18].

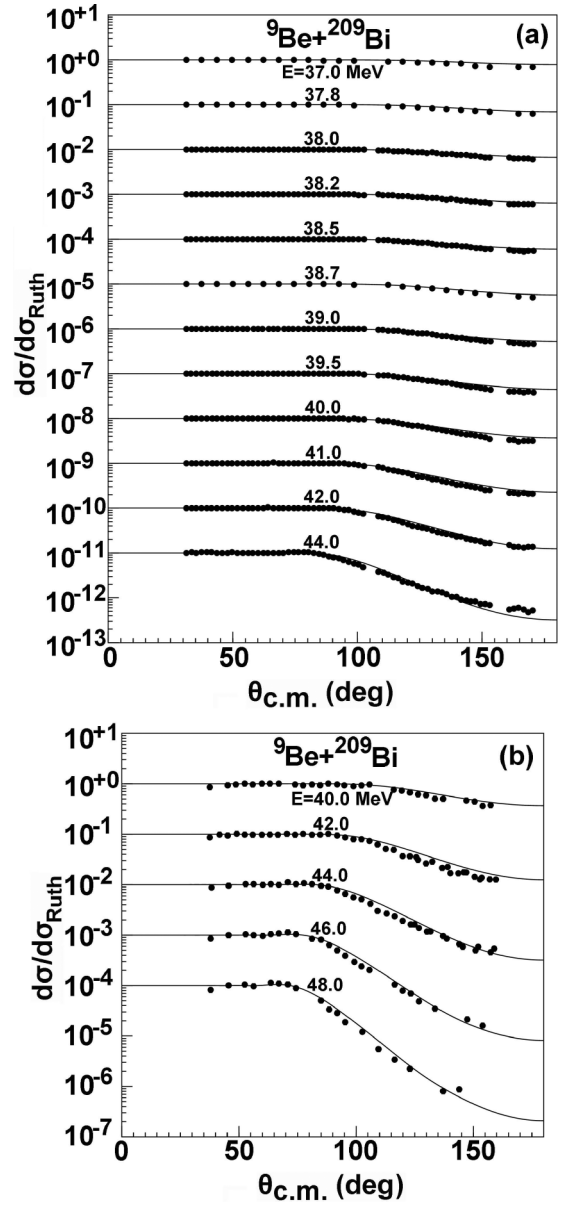

FIG. 11. The same as Fig. 2, but for ^{209}Bi [18,19].

the calculations and the data [17]. It is observed that the calculations are consistent with the experimental data [17] except for 68.0 and 75.0 MeV, where the theoretical results are slightly larger than the measurements above about 60°.

Furthermore, the elastic-scattering angular distributions of ^{208}Pb are also compared with the other experimental data [18] at incident energies from 37.0 to 50.0 MeV, which is shown in Fig. 10. One sees that the theoretical results are also in reasonable agreement with the experimental data in the range of the allowable error.

A similar analysis is also applied to the elastic-scattering angular distributions for the nearby nucleus ^{209}Bi. The calculations of elastic-scattering angular distributions are also compared with the data measured from different experiments. The results are shown in Fig. 11. Figure 11(a) plots the comparisons of calculations with the experimental data [18] at incident energies from 37.0 to 44.0 MeV. The overall agreement between the theoretical calculations and the experimental data is fairly good. Figure 11(b) presents the calculated angular distributions along with the experimental data [19] and the reasonable agreement is also obtained between them.

There are still a few experimental data of elastic-scattering angular distributions for ^{58}Ni and ^{nat}Ag targets at some energies. Figure 12 shows the comparisons of calculations with the data [5] for ^{58}Ni at incident energies of 20.0 and 26.0 MeV. One sees that the calculations are consistent with the data at incident energies of 20.0 MeV. While the calculations at incident energies of 26.0 MeV are slightly larger than the data from 50° to 80°. In this figure, the comparison of calculations for ^{107}Ag with the data [5] is also presented at incident energies of 26.0 MeV. As can be seen, very good agreement is achieved between them.

Moreover, the total reaction cross section is also an important observable. It has long been of interest since it is

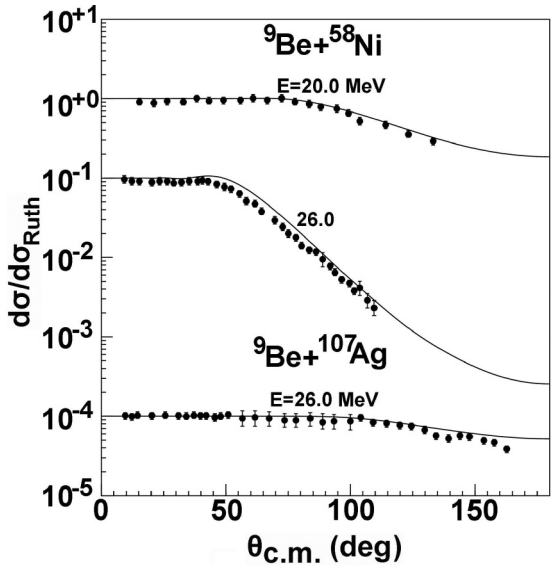

FIG. 12. The same as Fig. 2, but for ^{58}Ni and ^{nat}Ag [5].

intended to test nuclear models, get information about projectile matter distributions, and give clues to their structure. The accurate elastic-scattering measurement can determine the optical model potential parameters for a system, which in turn allow reaction cross sections to be deduced. So the reaction cross sections values can serve as important constraints in optical model analyses [28]. In particularly, the total reaction cross sections that are calculated with the optical model are important for the evaporation part of intranuclear cascade models and also for semiclassical pre-equilibrium models. All these nuclear models for the nonelastic channels rely on various other ingredients, such as discrete level schemes, level densities, γ-ray strength functions, fission barriers, etc. Uncertainties in those quantities all add to the total uncertainty of the calculated results. Therefore, it is crucial that the OMPs that enter such nuclear model calculations be adequately determined, from independent pieces of information [2]. In addition, the total reaction cross sections at low energies,

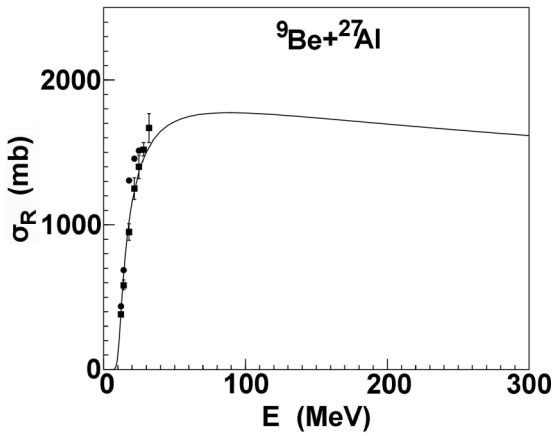

FIG. 13. Comparison between the optical model calculation and experimental data [20,21] of the ^{9}Be reaction cross sections for ^{27}Al.

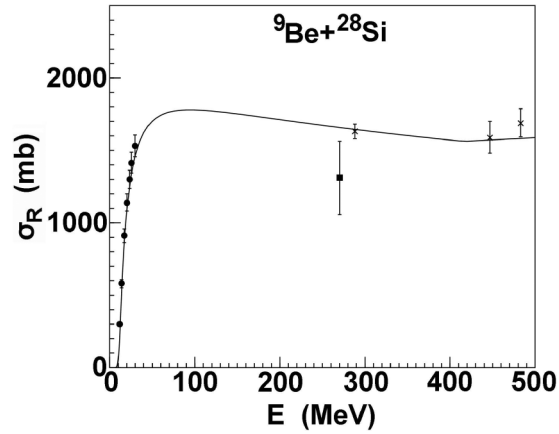

FIG. 14. The same as Fig. 13, but for ^{28}Si [7,22,23].

as it is known, are more sensitive to the surface structure of the nuclei, and the total reaction cross sections at high energies are more sensitive to the core part. So it is possible to investigate the structure of nuclei through the precise reaction cross sections at both high and low energies [29].

The reaction cross sections are also calculated using our global OMP for different targets and they are further compared with the existing experimental data. The reaction cross sections of ^{27}Al calculated using the obtained ^{9}Be global OMP are presented in Fig. 13. The comparison shows that very good fits are obtained between the theoretical results and the experimental data [20,21].

The reaction cross sections for the ^{28}Si target are calculated using the global OMP. The comparisons between the calculations and the corresponding data [7,22,23] are shown in Fig. 14. It can be seen that the global OMP of ^{9}Be can reproduce well the data [7] in the energy range from 12 to 30 MeV. In this figure, the reaction cross sections at 270.0, 288.0, 447.3, and 483.3 MeV are also predicted and compared with the experimental data [22,23]. In principle, the present model is not appropriate for extending predictions beyond 100 MeV. Here, we only perform a tentative calculation for the lighter target ^{28}Si. From the figure one can see that the

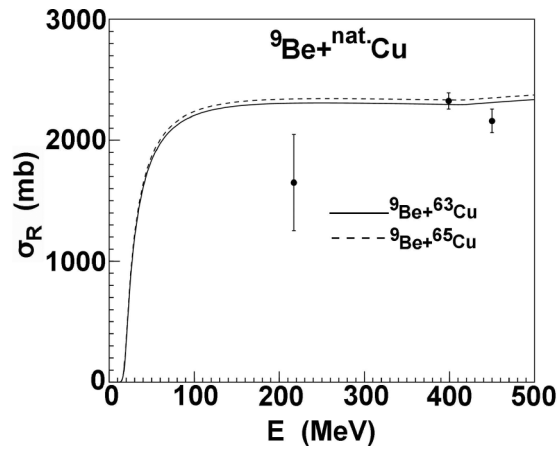

FIG. 15. The same as Fig. 13, but for ^{63,65}Cu [24].

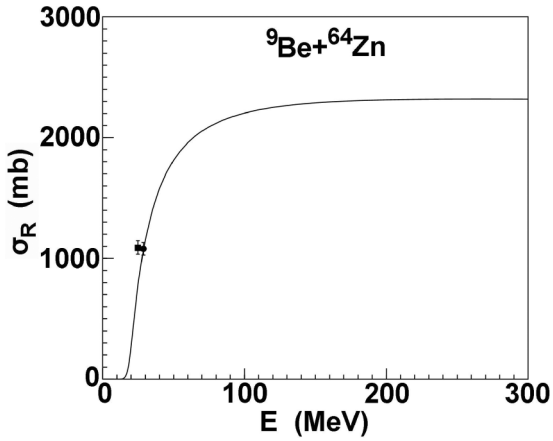

FIG. 16. The same as Fig. 13, but for ^{64}Zn [12,13].

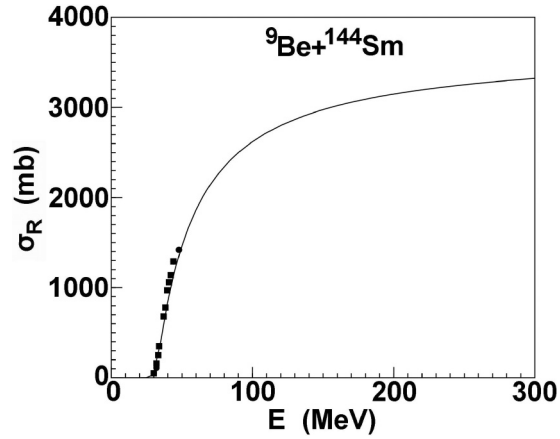

FIG. 18. The same as Fig. 13, but for ^{144}Sm [15,16].

prediction agrees well with the experimental data [22] at incident energies of 288.0, 447.3, and 483.3 MeV. While the result is larger than the measurement [23] at incident energies of 270.0 MeV.

The reaction cross sections for ^{63,65}Cu are also calculated using the global OMP. There are only experimental data of reaction cross sections for ^{nat}Cu above 200 MeV. Similarly, we compare the theoretical results with the existing experimental data [24]. Figure 15 shows the reasonable agreement is achieved between them.

For ^{64}Zn, the data of reaction cross sections were derived from the experimental elastic-scattering angular distributions for the ^{9}Be + ^{64}Zn systems [12,13] at incident energies of 28.4 and 28.97 MeV. The comparisons of calculations with the data are shown in Fig. 16. From the figure, it can be seen the calculations are in excellent agreement with the experimental data [13] at 28.97 MeV.

Furthermore, the reaction cross sections for ^{89}Y are compared with the corresponding data. These data are extracted from the elastic-scattering angular distributions for the ^{9}Be + ^{89}Y systems at sub- and near-barrier energies [25]. The good agreement is achieved between them, which is shown in Fig. 17.

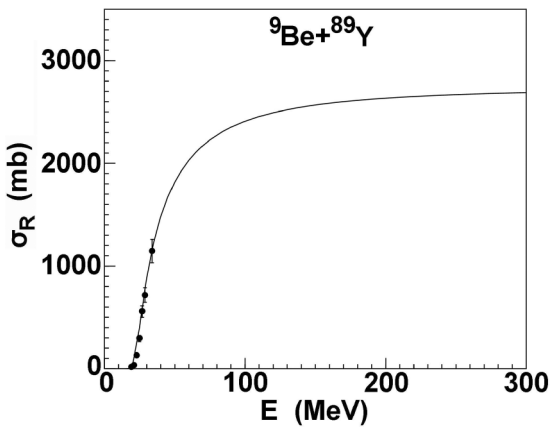

FIG. 17. The same as Fig. 13, but for ^{89}Y [25].

Figure 18 shows the calculations of reaction cross sections for ^{144}Sm. These results are further compared with the corresponding data. The calculations are also in satisfactory agreement with the data extracted from the measured elastic-scattering angular distributions for the ^{9}Be + ^{144}Sm systems [15,16].

To emphasize the differences of the weakly bound systems relative to the tightly bound system, we compare total reaction cross sections calculated for different systems. Among these systems we have combinations of stable weakly bound ^{9}Be, ^{6,7}Li [30,31]; halo nuclei ^{6,8}He [32]; and tightly bound ^{11}B [33] projectiles on the same medium mass target ^{89}Y. We also include the total reaction cross sections of ^{4}He projectile [34]. In order to make a consistent comparison, we used the existing global OMPs of different projectiles obtained by the same methods. In addition, as was done in Ref. [35], a suitable scaling of the results is made by dividing the cross sections by the factor $(A_p^{1/3} + A_T^{1/3})^2$ and the energy by the factor $Z_pZ_T/(A_p^{1/3} + A_T^{1/3})$, where $Z_p(Z_T)$ and $A_p(A_T)$ are the charge and mass numbers of the projectile (target), respectively. Figure 19 shows the results of total reaction

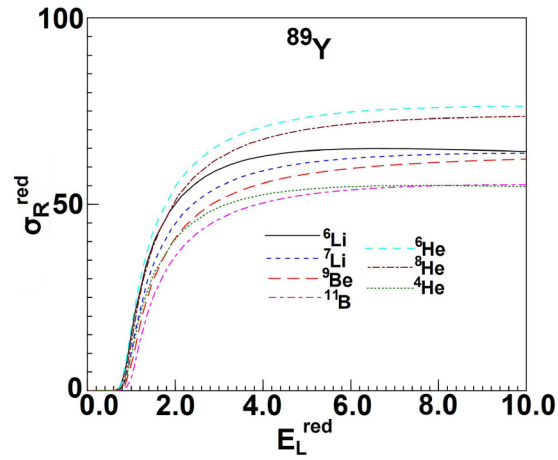

FIG. 19. Comparison of total reaction cross sections for different projectiles on medium mass target ^{89}Y.

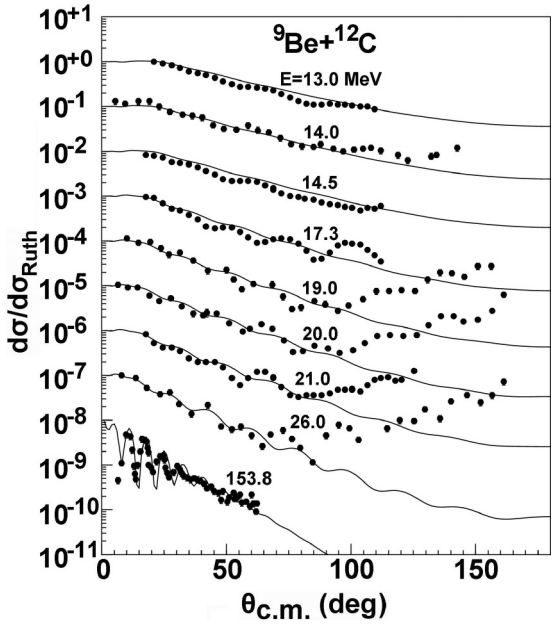

FIG. 20. Comparison between the optical model prediction and experimental data [37–39] of ^{9}Be elastic-scattering angular distributions for ^{12}C.

cross sections for different systems. One can see that the total reaction cross sections for the systems involving weakly bound nuclei ^{9}Be and ^{6,7}Li are higher compared to those involving the tightly bound nucleus ^{11}B and cluster projectile ^{4}He. The observed enhancement in the total reaction cross sections for weakly bound nucleus indicates that in addition to possible nonelastic channels as in the tightly bound nuclei, the extra contribution to the reaction cross sections must come

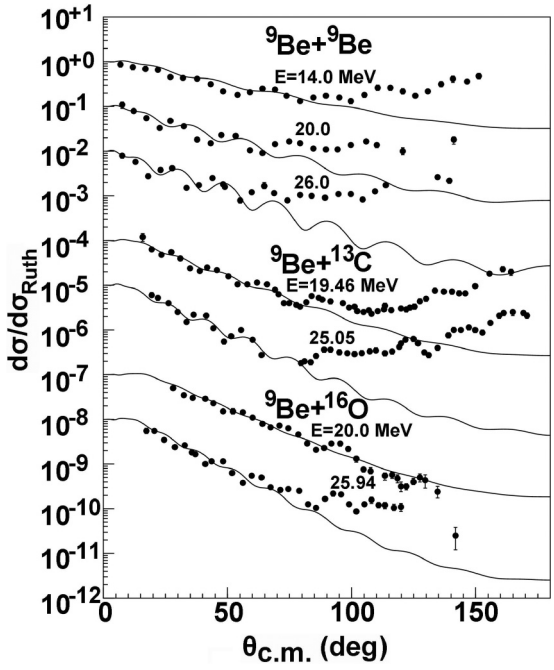

FIG. 21. The same as Fig. 19, but for ^{9}Be, ^{13}C, and ^{16}O [38,40].

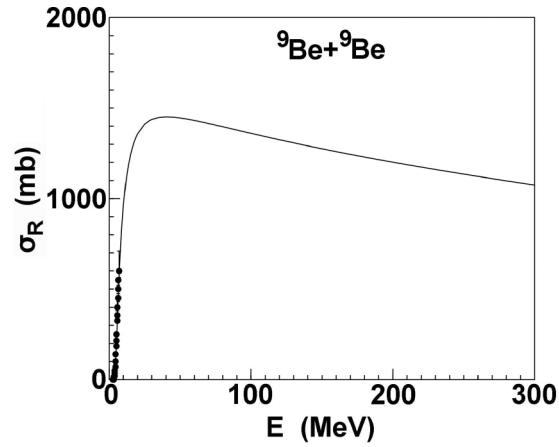

FIG. 22. Comparison between the optical model prediction and experimental data [44] of ^{9}Be reaction cross sections for ^{9}Be.

from the weakly bound nature of the nuclei due to the breakup channel being one the dominant reaction channels [14]. In addition, the total reaction cross sections for halo nuclei ^{6,8}He are highest among the systems presented in Fig. 19. The reason may be that Coulomb polarization favors neutrons in the halo residing in the region between the core and the target, which then enhances the reaction probabilities [36].

On the other hand, the elastic-scattering angular distributions for those targets in the mass number range $9 \leqslant A \leqslant 20$ are further predicted at different incident energies. These targets are lighter than the above-mentioned targets and the nuclear structure effect is expected to be more important for them. Figure 20 shows that the elastic angular distributions predicted by using the global OMP are in comparison with the data [37–39] for ^{12}C.

In addition, there are some targets measured for the elastic-scattering angular distributions at several energy points. The comparisons of theoretical calculations with the measurements [38,40] for ^{9}Be, ^{13}C, and ^{16}O targets are shown in Fig. 21.

From the comparisons with the existing experimental data for these lighter targets, it is found that the obtained global

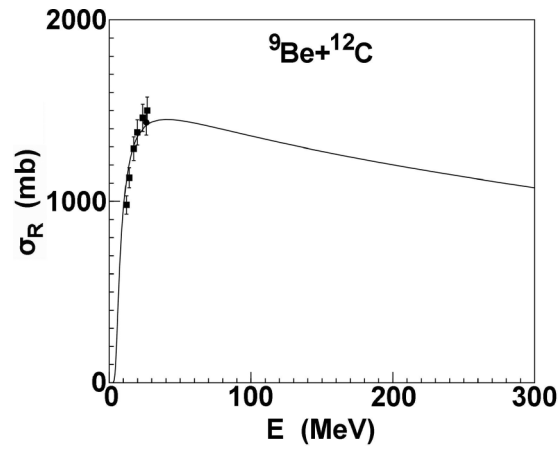

FIG. 23. The same as Fig. 22, but for ^{12}C [45,46].

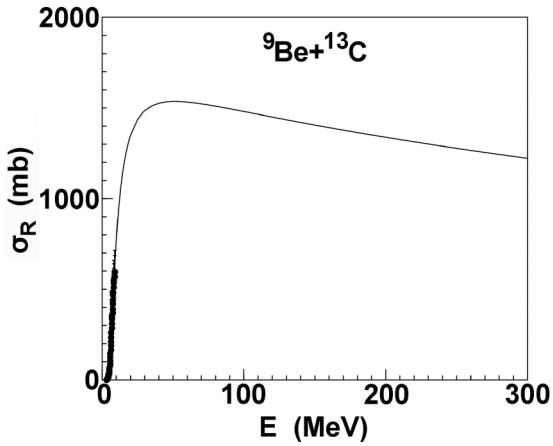

FIG. 24. The same as Fig. 22, but for ^{13}C [47].

OMP of ^{9}Be can be well reproduced with the measured angular distributions in the forward angular range (up to 80°) below 100 MeV. Unfortunately, the predictions are not completely consistent with the experimental data in backward-angle area where the experimental data have a pronounced upward trend. This behavior is typically observed in systems where projectile and target present the same core structure. It is known that ^{9}Be is a strongly deformed Borromean nucleus with a neutron threshold energy of 1.67 MeV and no bound excited state. The ^{9}Be breaks up into $^{8}\mathrm{Be}+n$, and the ^{8}Be is an unstable isotope and decays into two α particles with a half-life of 0.7 fs. Owing to the small breakup separation energies, reactions with the weakly bound projectile ^{9}Be show a strong breakup coupling, particularly below the barrier energy, that has an important effect on fusion and other reaction processes [41]. So the transitions from the inelastic to the elastic scattering channel and the transfer mechanism of ^{9}Be should be considered at lower incident energies [37,42,43]. In addition, the core structure effect should be also considered at energies near the Coulomb barrier. For example, the ^{12}C was considered as a cluster structure, composed of a ^{9}Be core and a ^{3}He valence particle in a single-particle state [37]. In the future work, we will particularly study the reaction mechanism for those lighter mass targets ($A \leqslant 20$) using the coupled discretized continuum channel (CDCC) method to improve the description of angular distributions at backward angles. On the other hand, it can be seen that the obtained ^{9}Be global phenomenological OMP can reproduce the ^{9}Be elastic angular distributions from the ^{12}C target at 153.8 MeV [39]. So it is still reliable for lighter targets when the incident energy is higher, which also means that the contributions of other reaction mechanisms may be relatively weak at higher incident energies.

Moreover, the reaction cross sections for these lighter targets are further predicted and compared with the experimental data. Figures 22 to 24 give the comparisons of reaction cross sections predicted by the obtained ^{9}Be global OMP with the corresponding experimental data [44–47] for ^{9}Be, and ^{12,13}C at different incident energies. The satisfactory agreements are presented between them.

IV. SUMMARY AND CONCLUSIONS

We present a new set of ^{9}Be global phenomenological energy-dependent optical potential parameters based on the form of the traditional Woods-Saxon potential within the framework of the optical model. It is obtained by fitting the experimental elastic-scattering angular distributions and reaction cross sections for the target mass numbers from 24 to 209 at incident energies below 100 MeV. Based on the present comparisons of the elastic scattering observables with the experimental data for the ^{9}Be projectile, it is clearly shown that the global OMP of the ^{9}Be projectile provide a good overall data description of the elastic scattering and reaction cross sections below 100 MeV for different targets. To check the reliability of the global OMP, the elastic-scattering angular distributions and reaction cross sections are further predicted using the global OMP for those targets in the mass number range $9 \leqslant A \leqslant 20$. Comparisons with the experimental data show that the theoretical results are in good agreement with the existing experimental data in the forward angular region. However, there is a pronounced disagreement at backward angles below 100 MeV, which suggests that the other reaction mechanisms need to be considered in the calculations, such as the transfer process. To improve the calculations, we will particularly study the reaction mechanism for those lighter mass targets ($A \leqslant 20$) using the coupled discretized continuum channel (CDCC) method in future work.

ACKNOWLEDGMENTS

This work was supported by the National Natural Science Foundation of China under Grants No. 11405099 and 11575291. This work is also a part of IAEA Coordinated Research Projects (CRPs) on Recommended Input Parameter Library (RIPL) for Fission Cross Section Calculations under Contract No. 20464.

[1] P. E. Hodgson, *The Optical Model of Elastic Scattering* (Clarendon, Oxford, 1963).
[2] A. J. Koning and J. P. Delaroche, Nucl. Phys. A **713**, 231 (2003).
[3] A. Gómez Camacho, E. F. Aguilera, and A. M. Moro, Nucl. Phys. A **762**, 216 (2005).
[4] P. R. S. Gomes, M. D. Rodríguez, G. V. Martí, I. Padron, L. C. Chamon, J. O. Fernández Niello, O. A. Capurro, A. J. Pacheco, J. E. Testoni, A. Arazi *et al.*, Phys. Rev. C **71**, 034608 (2005).
[5] R. Balzer, M. Hugi, B. Kamys, J. Lang, R. Müller, E. Ungricht and J. Unternährer, Nucl. Phys. A **293**, 518 (1977).
[6] P. R. S. Gomes, R. M. Anjos, C. Muri, J. Lubian, I. Padron, L. C. Chamon, R. Liguori Neto, N. Added, J. O. Fernándes Niello, G. V. Martí, O. A. Capurro, A. J. Pacheco, J. E. Testoni, and D. Abriola, Phys. Rev. C **70**, 054605 (2004).

[7] K. Bodek, M. Hugi, J. Lang, R. Mueller, E. Ungricht, K. Jankowski, W. Zipper, L. Jarczyk, A. Strzalkowski, G. Willim, and H. Witala, Nucl. Phys. A **339**, 353 (1980).

[8] M. S. Zisman, J. G. Cramer, D. A. Goldberg, J. W. Watson, and R. M. DeVries, Phys. Rev. C **21**, 2398 (1980).

[9] J. S. Eck, T. R. Ophel, P. D. Clark, and D. C. Weisser, Nucl. Phys. A **334**, 519 (1980).

[10] D. P. Stahel, G. J. Wozniak, M. S. Zisman, B. D. Jeltema, and J. Cerny, Phys. Rev. C **16**, 1456 (1977).

[11] S. B. Moraes, P. R. S. Gomes, J. Lubian, J. J. S. Alves, R. M. Anjos, M. M. Sant'Anna, I. Padrón, C. Muri, R. Liguori Neto, and N. Added, Phys. Rev. C **61**, 064608 (2000).

[12] A. Di Pietro, G. Randisi, V. Scuderi, L. Acosta, F. Amorini, M. J. G. Borge, P. Figuera, M. Fisichella, L. M. Fraile, J. Gomez-Camacho *et al.*, Phys. Rev. Lett. **105**, 022701 (2010).

[13] V. Scuderi, A. Di Pietro, L. Acosta, F. Amorini, M. J. G. Borge, P. Figuera, M. Fisichella, L. M. Fraile, J. Gomez-Camacho, H. Jeppesen *et al.*, edited by J. A. Caballero, C. E. Alonso, M. V. Andrés, J. E. García Ramos, and F. Pérez-Bernal, in *LA RÁBIDA 2009, International Scientific Meeting on Nuclear Physics: Basic Concepts in Nuclear Physics: Theory, Experiments And Applications*, AIP Conf. Proc. No. 1231 (AIP, Melville, NY, 2010), p. 191.

[14] C. S. Palshetkar, S. Santra, A. Shrivastava, A. Chatterjee, S. K. Pandit, K. Ramachandran, V. V. Parkar, V. Nanal, V. Jha, B. J. Roy *et al.*, Phys. Rev. C **89**, 064610 (2014).

[15] P. R. S. Gomes, J. Lubian, B. Paes, V. N. Garcia, D. S. Monteiro, I. Padron, J. M. Figueira, A. Arazi, O. A. Capurro, L. Fimiani *et al.*, Nucl. Phys. A **828**, 233 (2009).

[16] P. R. S. Gomes, I. Padron, E. Crema, O. A. Capurro, J. O. Fernandez Niello, A. Arazi, G. V. Marti, J. Lubian, M. Trotta, A. J. Pacheco *et al.*, Phys. Rev. C **73**, 064606 (2006).

[17] R. J. Woolliscroft, B. R. Fulton, R. L. Cowin, M. Dasgupta, D. J. Hinde, C. R. Morton, and A. C. Berriman, Phys. Rev. C **69**, 044612 (2004).

[18] N. Yu, H. Zhang, H. Jia, S. Zhang, M. Ruan, F. Yang, Z. Wu, X. Xu, and C. Bai, J. Phys. G **37**, 075108 (2010).

[19] C. Signorini, A. Andrighetto, J. Y. Guo, M. Ruan, L. Stroe, F. Soramel, K. E. G. Lobner, L. Muller, D. Pierroutsakou, M. Romoli *et al.*, Nucl. Phys. A **701**, 23 (2002).

[20] G. V. Marti, P. R. S. Gomes, M. D. Rodriguez, J. O. Fernandez Niello, O. A. Capurro, A. J. Pacheco, J. E. Testoni, M. Ramirez, A. Arazi, I. Padron *et al.*, Phys. Rev. C **71**, 027602 (2005).

[21] E. A. Benjamim, A. Lepine-Szily, D. R. Mendes, Jr, R. Lichtenthaler, V. Guimaraes, P. R. S. Gomes, L. C. Chamon, M. S. Hussein, A. M. Moro, A. Arazi *et al.*, Phys. Lett. B **647**, 30 (2007).

[22] R. E. Warner, M. H. McKinnon, J. S. Needleman, N. C. Shaner, F. D. Becchetti, D. A. Roberts, A. Galonsky, R. M. Ronningen, M. Steiner, J. A. Brown *et al.*, Phys. Rev. C **64**, 044611 (2001).

[23] L. Jiaxing, G. Zhongyan, X. Guoqing, Z. Wenlong, S. Zhiyu, W. Jiansong, T. Wendong, W. Meng, C. Zhiqiang, W. Wusheng *et al.*, High Energy Phys. Nucl. **26**, 683 (2002).

[24] M. G. Saint-Laurent, R. Anne, D. Bazin, D. Guillemaud-Mueller, U. Jahnke, J. Gen Ming, A. C. Mueller, J. F. Bruandet, F. Glasser, S. Kox *et al.*, Z. Phys. A-Atomic Nuclei. **332**, 457 (1989).

[25] C. S. Palshetkar, S. Santra, A. Chatterjee, K. Ramachandran, Shital Thakur, S. K. Pandit, K. Mahata, A. Shrivastava, V. V. Parkar, V. Nanal *et al.*, EPJ Web Conf. **17**, 03006 (2011).

[26] Q. B. Shen, Nucl. Sci. Eng. **141**, 78 (2002).

[27] B. Alder, S. Fernbach, and M. Rotenberg, *Methods in Computational Physics* (Academic Press, New York, 1966).

[28] R. E. Warner, R. A. Patty, P. M. Voyles, A. Nadasen, F. D. Becchetti, J. A. Brown, H. Esbensen, A. Galonsky, J. J. Kolata, J. Kruse *et al.*, Phys. Rev. C **54**, 1700 (1996).

[29] G. W. Fan, M. Fukuda, D. Nishimura, X. L. Cai, S. Fukuda, I. Hachiuma, C. Ichikawa, T. Izumikawa, M. Kanazawa, A. Kitagawa *et al.*, Phys. Rev. C **90**, 044321 (2014).

[30] Y. Xu, Y. Han, J. Hu, H. Liang, Z. Wu, H. Guo, and C. Cai, Phys. Rev. C **97**, 014615 (2018).

[31] Y. Xu, Y. Han, J. Hu, H. Liang, Z. Wu, H. Guo, and C. Cai, Phys. Rev. C **98**, 024619 (2018).

[32] X. Su, Y. Han, H. Liang, Z. Wu, H. Guo, and C. Cai, Int. J. Mod. Phys. E **25**, 1650033 (2016).

[33] Y. Xu, H. Guo, Y. Han, and Q. Shen, Int. J. Mod. Phys. E **27**, 1850099 (2018).

[34] X. Su and Y. Han, Int. J. Mod. Phys. E **24**, 1550092 (2015).

[35] P. N. de Faria, R. Lichtenthäler, K. C. C. Pires, A. M. Moro, A. Lépine-Szily, V. Guimarães, D. R. J. Mendes, Jr., A. Arazi, M. Rodríguez-Gallardo, A. Barioni, V. Morcelle, M. C. Morais, O. Camargo, Jr., J. Alcantara Nuñez, and M. Assunção, Phys. Rev. C **81**, 044605 (2010).

[36] E. F. Aguilera, E. Martinez-Quiroz, D. Lizcano, A. Gómez-Camacho, J. J. Kolata, L. O. Lamm, V. Guimarães, R. Lichtenthäler, O. Camargo, F. D. Becchetti *et al.*, Phys. Rev. C **79**, 021601(R) (2009).

[37] R. A. N. Oliveira, N. Carlin, R. Liguori Neto, M. M. de Moura, M. G. Munhoz, M. G. del Santo, F. A. Souza, E. M. Szanto, A. Szanto de Toledo, and A. A. P. Suaide, Nucl. Phys. A **856**, 46 (2011).

[38] E. Ungricht, D. Balzer, M. Hugi, J. Lang, R. Muller, L. Jarczyk, B. Kamys, and A. Strzalkowski, Nucl. Phys. A **313**, 376 (1979).

[39] G. R. Satchler, C. B. Fulmer, R. L. Auble, J. B. Ball, F. E. Bertrand, K. A. Erb, E. E. Gross, and D. C. Hensley, Phys. Lett. B **128**, 147 (1983).

[40] L. Jarczyk, J. Okolowicz, A. Strzalkowski, K. Bodek, M. Hugi, J. Lang, R. Muller, and E. Ungricht, Nucl. Phys. A **316**, 139 (1979).

[41] A. Gómez Camacho, P. R. S. Gomes, J. Lubian, and I. Padrón, Phys. Rev. C **77**, 054606 (2008).

[42] A. T. Rudchik, O. A. Momotyuk, V. A. Ziman, A. Budzanowski, A. Szczurek, I. Skwirczyńska, S. Kliczewski, and R. Siudak, Nucl. Phys. A **662**, 44 (2000).

[43] A. Barbadoro, F. Pellegrini, G. F. Segato, L. Taffara, I. Gabrielli, and M. Bruno, Phys. Rev. C **41**, 2425 (1990).

[44] F. Lahlou, B. Cujec, and B. Dasmahapatra, Nucl. Phys. A **486**, 189 (1988).

[45] J. C. Zamora, V. Guimaraes, A. Barioni, A. Lepine-Szily, R. Lichtenthaler, P. N. de Faria, D. R. Mendes, Jr., L. R. Gasques, J. M. B. Shorto, V. Scarduelli *et al.*, Phys. Rev. C **84**, 034611 (2011).

[46] L. Jarczyk, B. Kamys, A. Magiera, J. Sromicki, A. Strzalkowski, G. Willim, Z. Wrobel, D. Balzer, K. Bodek, M. Hugi *et al.*, Nucl. Phys. A **369**, 191 (1981).

[47] B. Dasmahapatra, B. Cujec, and F. Lahlou, Nucl. Phys. A **427**, 186 (1984).